

Benchmark PIV database for the validation of CFD simulations in a transitional cavity flow

Sciacchitano, A.; Arpino, F.; Cortellessa, G.

DOI

[10.1016/j.ijheatfluidflow.2021.108831](https://doi.org/10.1016/j.ijheatfluidflow.2021.108831)

Publication date

2021

Document Version

Final published version

Published in

International Journal of Heat and Fluid Flow

Citation (APA)

Sciacchitano, A., Arpino, F., & Cortellessa, G. (2021). Benchmark PIV database for the validation of CFD simulations in a transitional cavity flow. *International Journal of Heat and Fluid Flow*, 90, Article 108831. <https://doi.org/10.1016/j.ijheatfluidflow.2021.108831>

Important note

To cite this publication, please use the final published version (if applicable). Please check the document version above.

Copyright

Other than for strictly personal use, it is not permitted to download, forward or distribute the text or part of it, without the consent of the author(s) and/or copyright holder(s), unless the work is under an open content license such as Creative Commons.

Takedown policy

Please contact us and provide details if you believe this document breaches copyrights. We will remove access to the work immediately and investigate your claim.

Green Open Access added to TU Delft Institutional Repository

'You share, we take care!' - Taverne project

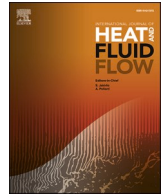
<https://www.openaccess.nl/en/you-share-we-take-care>

Otherwise as indicated in the copyright section: the publisher is the copyright holder of this work and the author uses the Dutch legislation to make this work public.



Contents lists available at ScienceDirect

International Journal of Heat and Fluid Flow

journal homepage: www.elsevier.com/locate/ijhff

Benchmark PIV database for the validation of CFD simulations in a transitional cavity flow

A. Sciacchitano^a, F. Arpino^b, G. Cortellessa^{b,*}

^a Aerospace Engineering Department, Delft University of Technology, Kluyverweg 1, 2629 HS Delft, Netherlands

^b Department of Civil and Mechanical Engineering, Università degli Studi di Cassino e del Lazio Meridionale, via G. Di Biasio 43, Cassino, Italy

ARTICLE INFO

Keywords:

Particle Image Velocimetry
CFD validation
RANS turbulence model
Uncertainty analysis
Transitional cavity
Benchmark in cavity flows

ABSTRACT

We present an experimental benchmark database for the transitional cavity flow. The database is obtained by planar Particle Image Velocimetry measurements at the median plane of the cavity model, for Reynolds numbers between 6300 and 19,000 based on the cavity height. A detailed uncertainty analysis of the experimental results is performed via the correlation statistics method for PIV uncertainty quantification and linear error propagation.

The experimental results are compared to two-dimensional Reynolds-Averaged Navier Stokes (RANS) numerical simulations with different turbulence models. It is shown that, when the standard $k-\omega$ turbulence model is employed, the discrepancy between numerical simulations and experimental results exceeds the uncertainty of the latter. Conversely, RANS simulations with the SST $k-\omega$ turbulence model agree well with the experimental data in terms of time-averaged flow properties; however, the turbulent kinetic energy results present significant discrepancies at all considered Reynolds numbers. The data presented in this paper is made available for open-access download via the 4TU.ResearchData repository with DOI: <https://doi.org/10.4121/14061233>.

1. Introduction

The significant developments of Computational Fluid Dynamics (CFD) technique in the last years have made this tool of investigation a valid support to experiments, allowing a significant reduction of tests' times and costs (Arpino et al., 2009). Numerical simulations can be used to investigate fluid flow characteristics in a wide range of applications, from the aerospace to the chemical and biomedical sectors (Arpino et al., 2015; Sheng et al., 1998), where extensive measurements are not possible, also allowing the optimisation of key design parameters (Westerweel et al., 2013).

However, despite the widespread use, CFD-based predictions may be affected by large errors if not properly verified and validated. These errors can be caused by a number of factors including the discretization of the domain, the proper selection of the boundary conditions (e.g. free-stream velocity and turbulence intensity, model geometry), or too restrictive assumptions in the mathematical modelling approach of the investigated physics (e.g. incompressible and isotherm fluid, Boussinesq hypothesis for turbulence modelling, etc.). Hence, a verification and validation procedure of any computer code is required before the code can be applied to practical problems (Oberkampf and Roy, 2011).

Unfortunately, the task of collecting experimental data for the validation of CFD simulations is far from trivial, as it requires the measurement of all relevant input data for the model (e.g. boundary conditions (BCs), geometry, thermophysical properties) and the useful system response quantities (SRQs), with their uncertainties (Smith, 2017).

In the last decades, Particle Image Velocimetry (PIV) has superseded laser Doppler anemometry and hot-wire anemometry as a tool to produce quantitative flow velocity data for the validation of numerical simulations. In the bio-medical community, Ford et al. (2008) made use of PIV experiments to validate unsteady CFD simulations in realistic cerebral aneurism models. By comparing experimental and numerical data, the authors showed the capability of their CFD simulations to accurately capture the cycle-to-cycle variations in the velocity field. DeBonis et al. (2010) used PIV data as reference velocity to validate CFD models in a shock wave boundary layer interaction flow, where the numerical simulations were conducted using RANS with several turbulence models, LES and DNS approaches. The authors noted that the CFD solutions were remarkably similar in the error levels, which suggests that errors due to the boundary conditions may be even larger than turbulence modelling assumptions and have a crucial role on the overall reliability of the prediction. The authors concluded that further research

* Corresponding author.

E-mail addresses: A.Sciacchitano@tudelft.nl (A. Sciacchitano), f.arpino@unicas.it (F. Arpino), g.cortellessa@unicas.it (G. Cortellessa).

<https://doi.org/10.1016/j.ijheatfluidflow.2021.108831>

Received 26 June 2020; Received in revised form 29 March 2021; Accepted 14 May 2021

Available online 29 May 2021

0142-727X/© 2021 Elsevier Inc. All rights reserved.

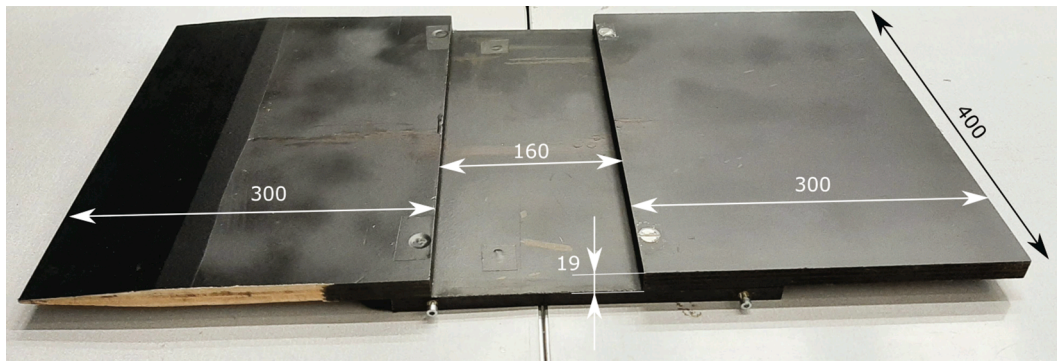


Fig. 1. Picture of the cavity model with dimensions in mm.

was needed for the validation of numerical simulations and that high-quality experimental data along with their uncertainty were crucial for this purpose. Using planar PIV data, Bengoechea et al. (2014) carried out a thorough validation of different RANS turbulence models (k - ϵ , k - ω and Reynolds Stress Transport Models RSTM) for the case of a swirling flow passing through a perforated screen. In their case, the RSTM gave the best agreement with the PIV velocity data, whereas the k - ϵ model strongly underestimated the peak axial and tangential velocity components.

In order to use experimental data for the validation of numerical simulations, detailed knowledge of the measurement uncertainty is required. Measurement errors in PIV have been thoroughly investigated a-priori in the last two decades, either via theoretical modelling of the measurements chain (Westerweel, 1997; Stanislas et al., 2004) or by Monte Carlo simulations on synthetic data (Fincham and Spedding, 1997; Foucaut et al., 2004). Most studies report that the errors of planar PIV measurements are in the range 0.03–1 pixels, depending on several factors, also including the image quality and the interrogation algorithm (Raffel et al., 2018). More recently, much emphasis has been given to the a-posteriori quantification of the measurement uncertainty (UQ), aiming at quantifying the uncertainty of each instantaneous velocity vector of a specific set of data (see Neal et al. (2015), Boomsma et al. (2016) for comparative assessments of different a-posteriori PIV-UQ approaches). Wilson and Smith (2013) and Sciacchitano and Wieneke, (2016) have extended the discussion to the propagation of the baseline uncertainty from instantaneous velocities to velocity derived flow properties, either statistical (e.g. time-averaged, turbulence kinetic energy TKE and Reynolds stresses) or instantaneous (e.g. vorticity and pressure). A detailed review of PIV uncertainty quantification methods is reported in Sciacchitano (2019).

Based on the above, it can be concluded that the PIV technique has reached a level of maturity that PIV data along with their uncertainty can be reliably employed for the validation of numerical simulations by CFD. In this work, a benchmark database for CFD validation is produced via PIV measurements of a transitional-type cavity flow. Flow measurements and simulations are conducted at free-stream velocities ranging from 5 m/s to 15 m/s, or Reynolds numbers from 6300 to 19,000, encompassing the cases of laminar and turbulent boundary layer prior to separation. All inputs required for the numerical model, namely boundary conditions and inflow velocity profiles, and the SRQs (time-averaged velocity field and the Reynolds stresses within the cavity) are measured and their uncertainty quantified. The transitional-type cavity flow case has been selected for this work due to three main reasons (Prasad and Koseff, 1989): i) due to the regular geometry and the ease in posing the boundary conditions, the cavity flow is a popular test case for validation of CFD results (see for instance Botella and Peyret (1998) and Ghia et al. (1982)); ii) the cavity flow is complex and not easy to predict, because it features a primary stationary vortex, secondary structures as corner vortices, a fixed separation point and an unsteady reattachment point; iii) the cavity flow is an idealized

representation of many engineering situations such as the flow over repeated slots on the surface of a vehicle or on the walls of heat exchangers. Furthermore, cavity flows offer a broad range of fluid mechanical interesting distinctive traits: unsteady shear layer developing from the leading edge, shedding and periodic behaviour, recirculation zones, instability and 3D effects.

2. Experimental setup

2.1. Experimental apparatus and data processing

Experiments are conducted in the W-tunnel of the Delft University of Technology. The W-Tunnel is an open-circuit, open test section wind tunnel with a squared cross-section of $40 \times 40 \text{ cm}^2$ and 9:1 area contraction. The free-stream velocity reaches a maximum value of about 35 m/s and can be regulated by setting the revolutions per minute of the centrifugal fan. The free-stream turbulence intensity is about 0.5%. The wind tunnel model is a cavity made out of wood and spanning the entire test section width. The height and length of the cavity are $H = 19 \text{ mm}$ and $L = 160 \text{ mm}$, respectively, yielding a cavity aspect ratio of $AR = L/H = 8.42$, which classifies the cavity as transitional (Atvars et al., 2009). The front plate leading edge comprises a modified elliptical profile to avoid flow separation. A picture of the model with dimensions in millimetres is shown in Fig. 1. Measurements are conducted at free-stream velocities of 5.27 m/s, 10.58 m/s, and 16.15 m/s, resulting in Reynolds numbers Re_H of 6300, 12,500 and 19,000, respectively, based on the height of the cavity.

The illumination is provided by a dual-cavity Quantel EverGreen laser. The laser beam is shaped into a 2 mm thick sheet by means of a combination of spherical and cylindrical lenses. The laser sheet thickness is measured by visual inspection by placing a millimetre paper in the light sheet. An orange marker is applied on the millimetre paper to make the laser light reflection visible when wearing band-stop filter protective goggles. The flow is seeded with micrometric water-glycol droplets produced by a SAFEX seeding generator (1 μm median diameter).

Images are acquired with a LaVision Imager Pro LX 16 M camera (CCD sensor, 12 bit, 4872×3248 pixels, 7.4 μm pixel pitch). For the measurements of the flow inside the cavity, the camera is equipped with a Nikkor lens of 60 mm focal length, set at numerical aperture $f\# = 8$. The sensor is cropped to 4744×1356 pixels to achieve an acquisition frequency of about 1.5 Hz in time-straddling mode. The camera images a region of $198 \times 56 \text{ mm}^2$ comprising the cavity. The resulting magnification factor is $M = 0.18$, yielding a digital image resolution of 42 $\mu\text{m}/\text{px}$. A time separation of $\Delta t = 45 \mu\text{s}$ between laser pulses is selected to obtain a particle image displacement of about 10 pixels in the free-stream. A set of 6500 uncorrelated image pairs is recorded to ensure the convergence of the flow statistics. Additionally, dedicated boundary layer measurements at a distance $5.3H$ upstream the cavity are conducted. For the boundary layer experiments, the camera mounts a

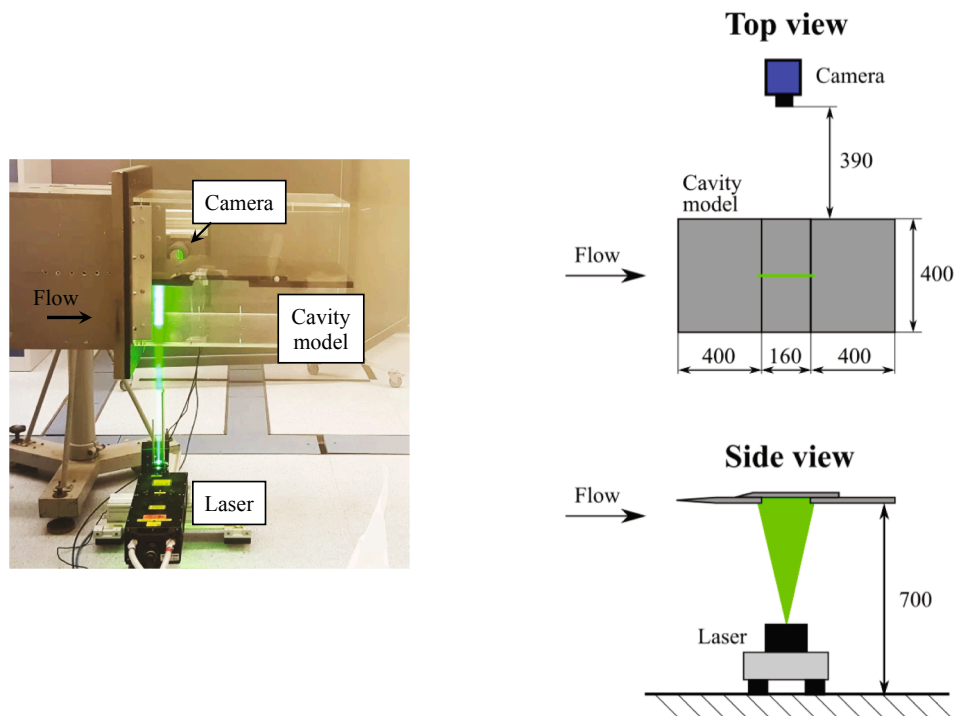


Fig. 2. Setup of the PIV measurements. Left: picture of the experimental setup; right: sketches of the top and side views, with dimensions in millimeters (in the side view, for sake of clarity the camera is not shown).

Table 1
Experimental parameters.

Parameter	Cavity Flow Measurements	Boundary Layer Measurements
Illumination	Quantel Evergreen Nd:YAG laser (200 mJ pulse energy, wavelength $\lambda = 532$ nm, maximum repetition frequency of 15 Hz)	
Seeding system	SAFEX seeding generator (water-glycol droplets of 1 μm median diameter)	
Imaging	LaVision Imager Pro LX 16 M camera (CCD sensor, 12 bit, 4872×3248 pixels, 7.4 μm pixel pitch)	
Lens focal length	60 mm	200 mm
Numerical aperture ($f\#$)	8	8
Active sensor size	4744×1356 pixels	1624×3084 pixels
Field of view	198×56 mm ²	21.2×40.3 mm ²
Magnification factor (M)	0.18	0.56
Digital image resolution	42 $\mu\text{m}/\text{px}$	13 $\mu\text{m}/\text{px}$
Inter-frame time separation	45 μs	13 μs
Number of recordings	6500	1500
Seeding density (particles per pixel, ppp)	0.075	0.050
Acquisition frequency	1.5 Hz	1.5 Hz
Air pressure	1026.7 ± 1.5 hPa	1028.7 ± 1.5 hPa
Air temperature	292.1 ± 0.9 K	291.4 ± 0.2 K
Air humidity	$55.3 \pm 5.0\%$	$41.0 \pm 1.0\%$
Air density	1.219 ± 0.004 kg/m ³	1.226 ± 0.002 kg/m ³

Nikkor lens of 200 mm focal length, set at numerical aperture $f\# = 8$. The sensor size is cropped to 1624×3084 pixels and the magnification factor is $M = 0.56$, yielding a digital image resolution of 13 $\mu\text{m}/\text{px}$. A set of 1500 images is acquired in time-straddling mode with an inter-frame time separation of $\Delta t = 13$ μs .

The atmospheric pressure, temperature and air humidity are monitored during the experiments with an Alecto Weather Station 1500. The resolution uncertainty is 100 Pa, 0.1 K and 1% for air pressure, temperature and relative humidity, respectively. The total uncertainties of these air properties are computed as the Euclidean norm between the

Table 2
Processing parameters.

Parameter	Cavity Flow Measurements	Boundary Layer Measurements
Interrogation window size	16×16 pixels	16×16 pixels
Number of passes	3	3
Interrogation window shape	Gaussian	Elliptical 4:1
Overlap factor	75%	75%
Vector pitch	168 μm	52 μm
Dynamic Spatial Range (DSR)	300	400
Dynamic Velocity Range (DVR)	100	100

resolution uncertainties and the standard deviation over repeated measurements, with the latter multiplied by a coverage factor of 1.96 for 95% confidence level. The density of humid air is calculated by treating it as a mixture of perfect gases, namely dry air and water vapour (Davis, 1992). Its uncertainty is evaluated by propagating the uncertainties of air pressure, temperature and relative humidity via the Monte Carlo method (Coleman and Steele, 2018).

A picture of the experimental setup with sketches of the top and side views, and the parameters of the experiments are reported in Fig. 2 and Table 1, respectively.

Image acquisition and processing are conducted with the LaVision DaVis 8.3 software. The raw images are pre-processed via a subtraction of the minimum intensity in time over a sliding kernel of 7 images to remove the unwanted light reflections on the solid surface. The computation of the velocity fields is conducted with a multi-pass correlation based interrogation algorithm with window deformation (Scarano and Riethmuller, 2000). The processing parameters are summarized in Table 2. The dynamic spatial range (Adrian, 1997), computed as the ratio between the stream-wise direction of the field of view and the interrogation window linear size, is 300 for the cavity flow

Table 3
Model validation experiment completeness table.

Attributes	Level of completeness				Attribute score
	Level 0	Level 1	Level 2	Level 3	
Experimental facility		Assessed			1
Analog instrumentation and signal processing			Assessed		2
Boundary and initial conditions		Assessed			1
Fluid and material properties			Assessed		2
Test conditions		Assessed			1
System response quantities			Assessed		2

measurements and 400 for the boundary layer measurements. The dynamic velocity range (DVR) is evaluated as the ratio between the maximum velocity measured and the velocity uncertainty and is equal to 100 in both measurements.

2.2. PIV data uncertainty quantification

Following Coleman and Steele (Coleman and Steele, 2018), the total uncertainty is expressed as:

$$U_{tot} = \sqrt{B^2 + U^2} \quad (1)$$

where B is the systematic (bias) uncertainty and U is the random standard uncertainty. When they stem from multiple individual contributions, both B and U are computed as the root of the sum of the squares of the individual bias and random contributions, respectively.

The random uncertainty of the flow quantities measured by PIV (namely time-averaged velocity, Reynolds stresses and Turbulent Kinetic Energy) is quantified following the approach discussed by Sciacchitano and Wieneke (2016). The expanded random uncertainty of the time-averaged streamwise velocity component \bar{u} is estimated as (an analogous equation applies to the vertical velocity component):

$$U_{\bar{u}} = \frac{k s_u}{\sqrt{N}} \quad (2)$$

where s_u is the sample standard deviation of the streamwise velocity component, N is the number of statistically uncorrelated samples, and k is the coverage factor. Assuming a Gaussian distribution of the PIV measurement errors (Neal et al., 2015), a coverage factor $k = 1.96$ is selected for a confidence level of 95%.

Systematic error sources may arise from pixel locking (Westerweel, 1997), evaluation of the image magnification and modulation effects due to the finite window size (Nogueira et al., 2005). In the present experiment, pixel locking errors are negligible (smaller than 0.1% of the measured particle image displacement) because the imaging system parameters (in particular M and $f\#$) were selected to yield a diffraction-based particle image diameter of about 2 pixels (Raffel et al., 2007). The uncertainty ascribed to the evaluation of the image magnification is estimated from repeated measurement as 0.2% of the local velocity. For the normal Reynolds stresses Re_{xx} , the random uncertainty is quantified as in Sciacchitano and Wieneke (2016); a similar equation applies for Re_{xy} :

$$U_{Re_{xx}} = k \left(Re_{xx} \sqrt{\frac{2}{N} + \overline{U_u^2}} \right) \quad (3)$$

where $\overline{U_u^2}$ is the mean square of the uncertainty of the instantaneous velocity, here evaluated via the correlation statistics method (Argyropoulos and Markatos, 2015).

The two-dimensional definition of the turbulence kinetic energy TKE is employed,

$$TKE = \frac{1}{2} (Re_{xx} + Re_{yy}) \quad (4)$$

The random uncertainty of the latter is retrieved via linear error propagation (Sciacchitano, 2019):

$$U_{TKE} = \frac{1}{2} \sqrt{U_{Re_{xx}}^2 + U_{Re_{yy}}^2} \quad (5)$$

The uncertainty of the Reynolds shear stresses $Re_{xy} = \overline{u'v'}$ is computed according to Sciacchitano and Wieneke (2016) as:

$$U_{Re_{xy}} = \sqrt{Re_{xx} Re_{yy} \left(\frac{1 + \rho_{xy}^2}{N - 1} \right)} \quad (6)$$

where $\rho_{xy} = Re_{xy} / \sqrt{Re_{xx} Re_{yy}}$ is the cross-correlation coefficient between the horizontal and vertical velocity components.

For the definition of the boundary layer properties such as boundary layer thickness, displacement thickness, momentum thickness and shape factor, knowledge of the uncertainty of the wall position is of paramount importance. In principle, the exact position of the wall can be determined from the raw PIV images, looking at the laser light reflection on the solid surface. However, the laser source generates a wide flare in the camera image, making it difficult to accurately identify the wall location. Hence, in the present work the wall location is determined by fitting a second order polynomial through the five velocity values closest to the wall, similarly to the approach reported by Harris et al. (2016). Based on the analysis of 27 independent time-averaged velocity profiles (9 independent locations around $x/H = -5$ at the three different free-stream velocities), it is found that the uncertainty of the wall location at 95% confidence level is $U_{ywall} = 0.10$ mm.

2.3. Model validation experiment completeness

Following Oberkampf and Roy (2011), the completeness of the current model validation experiment is summarized in a table that reports six experimental attributes and four level of completeness. The six experimental attributes are: experimental facility; analog instrumentation and signal processing; boundary and initial conditions; fluid and material properties; test conditions; system response quantities. Four levels of information are defined for each attribute, where level 0 corresponds to no or little description, and level 3 to the highest level of information provided. For further information on the definition of the experimental attributes and of the completeness levels, the interested reader is referred to (Oberkampf and Roy, 2011). The model validation experiment completeness table for the experiment presented in this work is shown in Table 3. It is shown that all experimental attributes have a level of completeness between 1 and 2. The detailed description of the PIV system, as well as of the fluid properties and system response quantities with their uncertainties, presented in Sections 2.1 and 2.2, allow to achieve a level 2 of completeness for those experimental attributes.

3. Numerical setup

The velocity and pressure fields in the cavity were numerically predicted by solving the mass and momentum conservation equations (Versteeg and Malalasekera, 2007; Lewis et al., 2004) under the

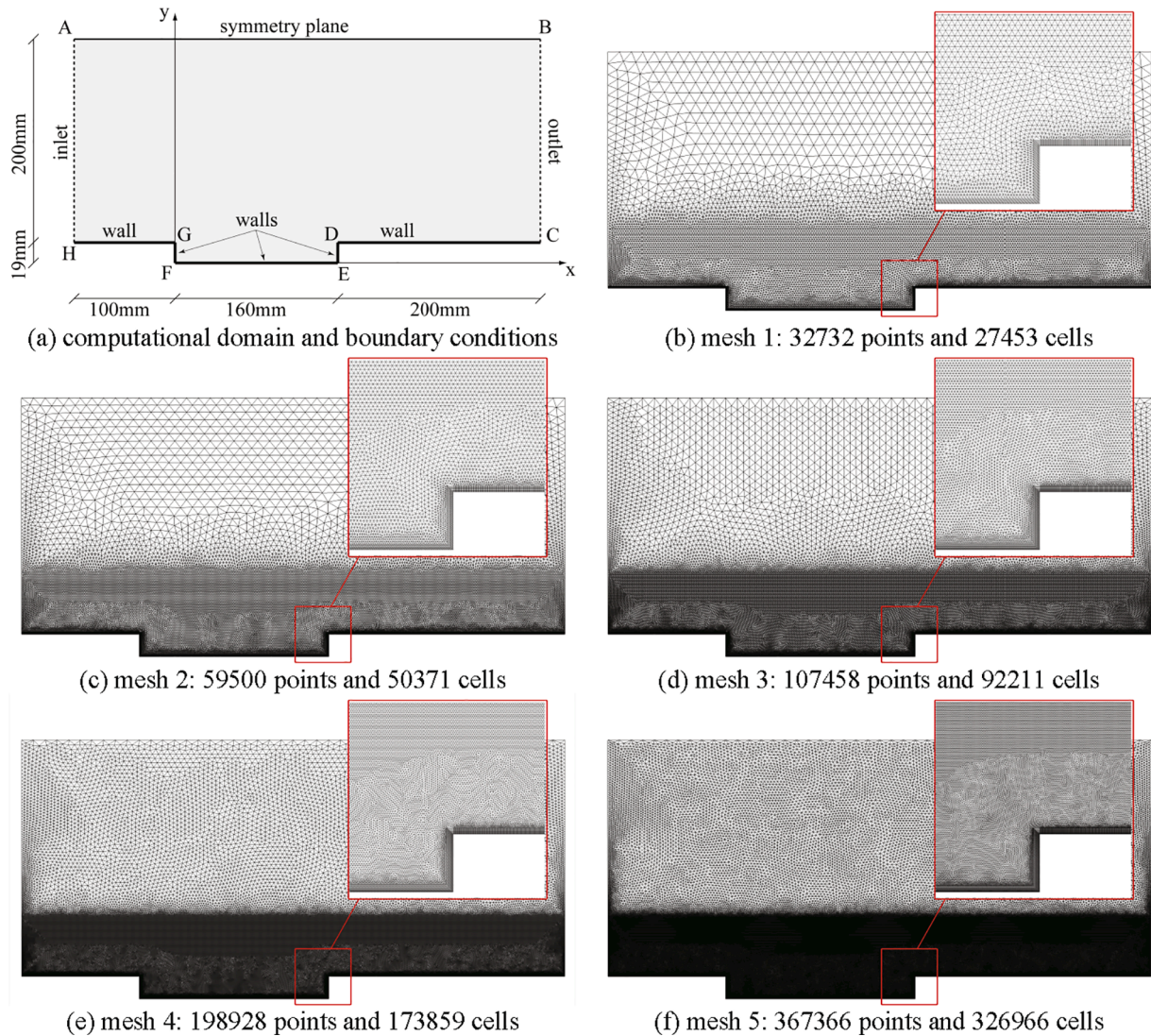


Fig. 3. Computational domain and boundary condition imposed for numerical simulations (a); computational grids employed for grid sensitivity analysis (from (b) to (f)).

Table 4

Details of the computational meshes.

Mesh #	Number of Points	Number of Cells
1	32,732	27,453
2	59,500	50,361
3	107,458	92,211
4	198,928	173,859
5	367,366	326,966

assumption of two-dimensional, steady, incompressible and isotherm flow with constant thermodynamic properties. Details about solved partial differential equations are available in the scientific literature (Arpino et al., 2014; Scungio et al., 2015) and are not reported here for brevity. Turbulence was modelled using the Reynolds-Averaged Navier Stokes (RANS) approach, solving the standard $k-\omega$ (Wilcox, 2008) and the Shear Stress Transport (SST) $k-\omega$ (Menter, 1993) RANS models, as the $k-\omega$ model is well suited for simulating fluid flow in the viscous sub-layer region (Arpino et al., 2017).

Governing Partial Differential Equations (PDEs) were numerically solved employing the open source OpenFOAM code, based on the finite volume formulation. The default second order Gauss linear interpolation scheme and the Geometric Agglomerated Algebraic Multigrid (GAMIG)

solver with a tolerance value equal to 10^{-6} were adopted. Numerical simulations were conducted using the Semi-Implicit Method for Pressure-Linked Equations (SIMPLE) (Versteeg and Malalasekera, 2007) with pseudo-time step value equal to 10^{-3} .

The computational domain and the boundary conditions employed alongside with main geometric dimensions are available in Fig. 3(a). The adopted geometry measures 219 mm of total height and 460 mm of length, with a step height, H, of 19 mm. The inlet section is located 100 mm (about 5.3H) upstream the leading edge of the cavity.

At the inlet section, the velocity and turbulent kinetic energy profiles measured by PIV were imposed, for three free-stream velocity values: 5.27 m/s, 10.58 m/s and 16.15 m/s. Besides, ω inlet profile was imposed at the inlet section of the computational domain, as calculated according

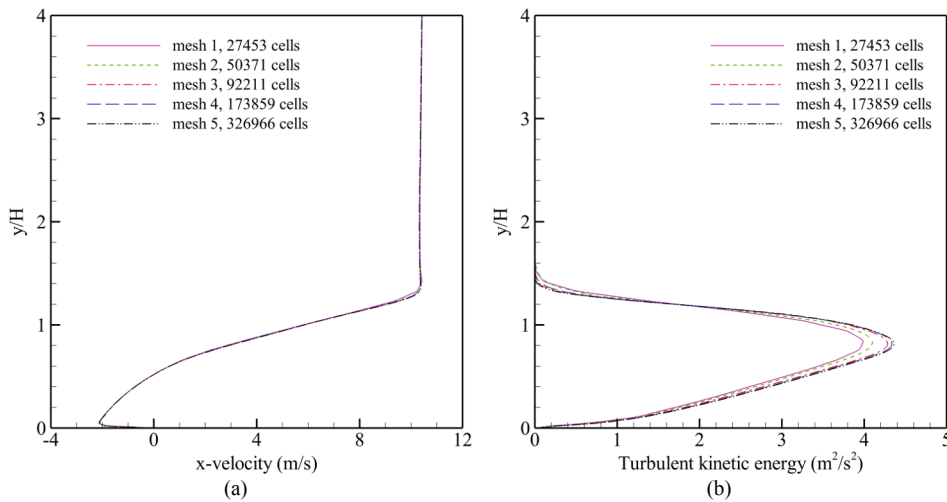


Fig. 4. Grid sensitivity analysis: (a) horizontal component of velocity profiles obtained in correspondence of $x/H = 4$; (b) turbulent kinetic energy profiles obtained in correspondence of $x/H = 4$.

to the following equation:

$$\omega = \frac{k^{0.5}}{0.038 \cdot l} \quad (7)$$

where l represents the mixing length, evaluated as 2% of the boundary layer thickness, whose value was experimentally determined. Zero pressure was imposed at the outlet section, located at a distance of 200 mm (about $10.5H$) downstream the trailing edge of the cavity. A symmetry boundary condition was imposed at the top side of the computational domain, located at $y = 219$ mm. No slip boundary condition was finally imposed on the solid walls.

The computational grid employed for the computations was constructed using the open source software Salome and was determined on the basis of a proper grid sensitivity analysis. In particular, five computational grids were considered, as reported in Fig. 3(b)–(f) and Table 4.

All the computational grids were refined near solid walls, with a first layer thickness of about 1×10^{-4} m, to properly capture the boundary layer. For each refinement step, the cells size was reduced to about one half and the total number of cells was about doubled. Fig. 4 shows the horizontal velocity profiles and turbulent kinetic energy profiles obtained with the grids reported in Fig. 3(b)–(f). The mesh chosen for the numerical simulation was the mesh 4, as results produced employing

this grid present a discrepancy lower than 1% with respect to results obtained using mesh 5.

Additional grid convergence tests were performed considering the Richardson error estimation procedure (Roache, 1997). Meshes 3, 4 and 5 were selected to evaluate the formal order of accuracy of the algorithm by Eq. (8):

$$p = \frac{\ln\left(\frac{f_3 - f_2}{f_2 - f_1}\right)}{\ln(r)} \quad (8)$$

where f_1 , f_2 and f_3 are numerical solutions obtained with grid spacing equal to h_1 , h_2 and h_3 respectively and r is the refinement factor adopted for the generation of the different grids.

Numerical grids, illustrated in Table 4, were obtained considering a constant refinement factor equal to 1.6. The average formal order of accuracy of the algorithm, obtained by Eq. (8), is equal to 1.52.

Finally, by Eqs. (9) and (10), the average error in a fine grid solution f_1 and in a course grid solution f_2 was determined:

$$E_{Mesh5}^{fine} = \frac{f_2 - f_1}{1 - r^p} \quad (9)$$

$$E_{Mesh4}^{course} = \frac{r^p (f_2 - f_1)}{1 - r^p} \quad (10)$$

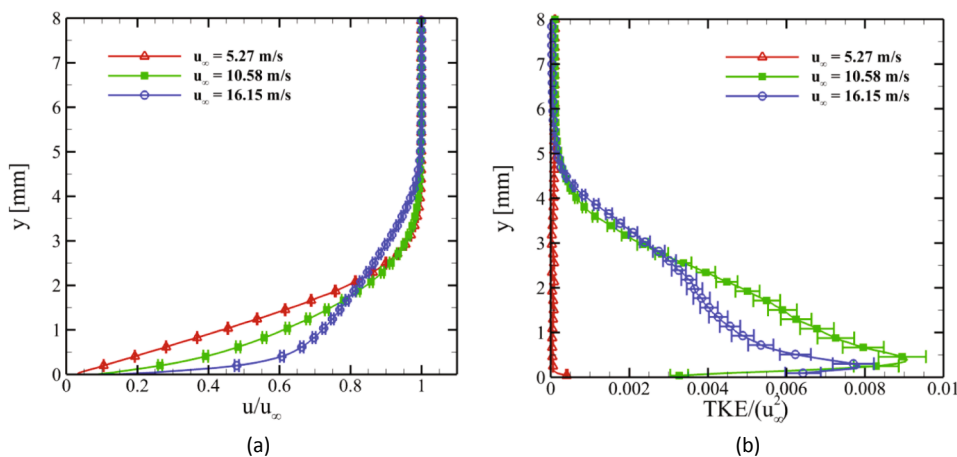


Fig. 5. Boundary layer profiles at $x/H = -5.3$. Left: time-averaged streamwise velocity. Right: turbulent kinetic energy. For sake of clarity, one every four symbols is plotted. The variable on the vertical axis (y) denotes the distance from the wall.

Table 5
Boundary layer properties.

u_∞ (m/s)	δ_{95} (mm)	δ_{95}/H	δ^* (mm)	δ^*/H	θ (mm)	θ/H	SF	u_τ (m/s)	Re_θ	Re_τ	C_f
5.27	2.87	0.151	1.24	0.065	0.50	0.026	2.48	0.30	176	58	0.007
10.58	2.94	0.155	0.94	0.050	0.53	0.028	1.79	0.85	374	168	0.013
16.15	3.65	0.192	0.83	0.044	0.58	0.031	1.43	1.43	624	348	0.016

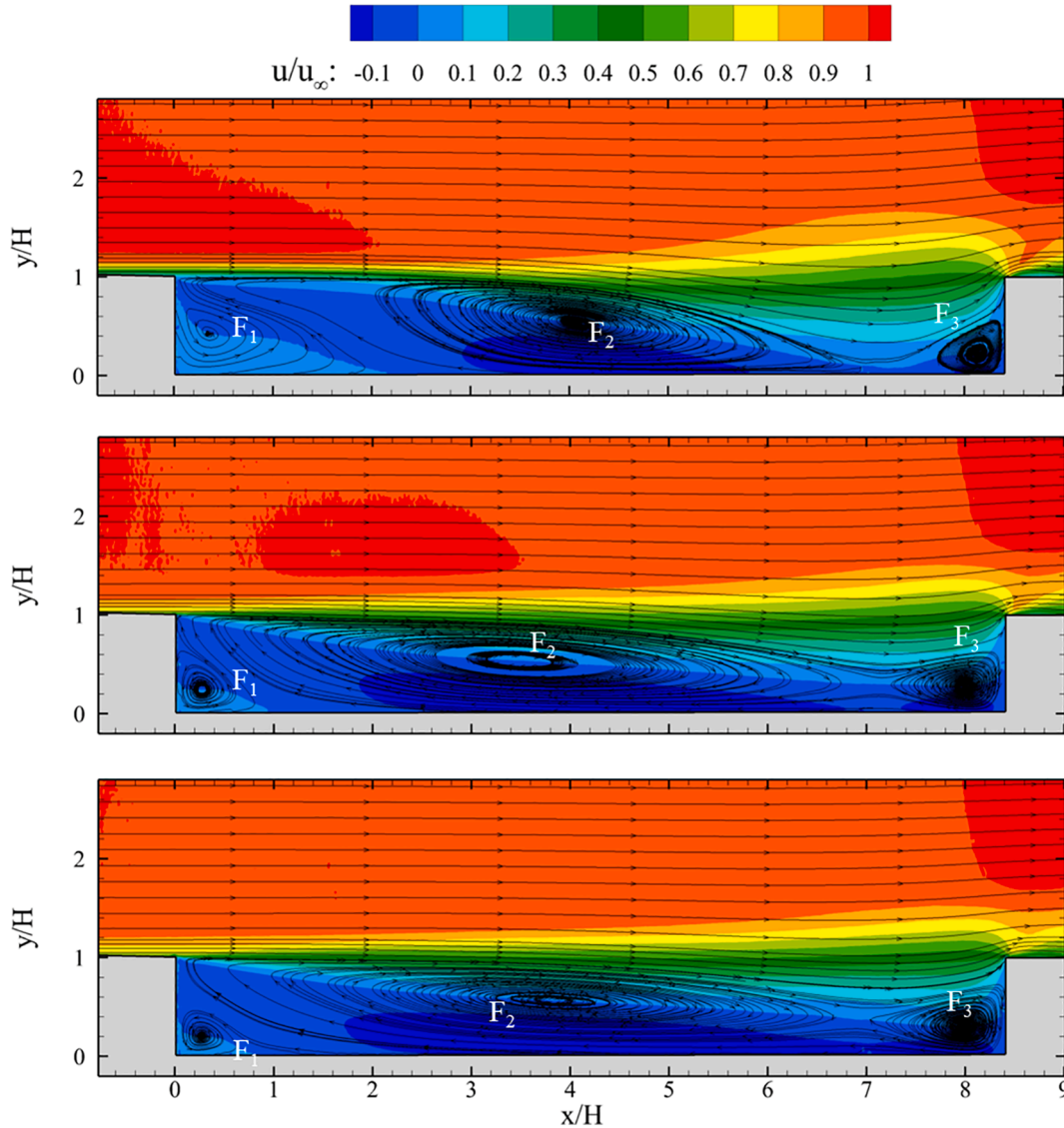


Fig. 6. Experimental time-averaged velocity fields. Top: $u_\infty = 5.27$ m/s; middle: $u_\infty = 10.58$ m/s; bottom: $u_\infty = 16.15$ m/s.

The average error obtained for Mesh 4, E_{Mesh4}^{course} , is equal to 0.89% while the average error obtained for Mesh 5, E_{Mesh5}^{fine} , is equal to 0.72%. Therefore, also this metric for the error estimation demonstrates that the selected computational grid (Mesh 4) presents an average error lower than 1%.

The average y^+ value obtained using mesh 4 is equal to 0.057 for a free stream velocity of 10.58 m/s.

4. Results

In this section, the experimental and numerical results are described in terms of: i) boundary layer before separation; ii) mean velocity field contour; iii) Turbulent Kinetic Energy (TKE) distribution; iv) uncertainty bounds of the measured quantities; v) numerical model validation in

terms of time-averaged velocity profiles and TKE.

4.1. Boundary layer before separation

The boundary layer profile prior to separation was measured via dedicated experiments. Fig. 5 illustrates the profiles of time-averaged velocity (left) and TKE (right) extracted at $x/H = -5.3$ obtained in correspondence of the three different free stream velocities (u_∞) equal to 5.27 m/s, 10.58 m/s and 16.15 m/s. The boundary layer profile is measured up to a distance of 30 μm from the wall, where the velocity is approximately $0.15u_\infty$. The main boundary layer properties, namely thickness δ_{95} , displacement thickness δ^* , momentum thickness θ , shape factor SF, skin friction velocity u_τ , momentum thickness Reynolds number (Re_θ), shear velocity Reynolds number (Re_τ) and skin friction

Table 6
Locations of the three foci at the three free-stream velocities. Experimental data.

u_∞ (m/s)	F_1		F_2		F_3	
	x/H	y/H	x/H	y/H	x/H	y/H
5.27	0.351	0.429	4.076	0.511	8.130	0.216
10.58	0.274	0.242	3.478	0.537	7.995	0.280
16.15	0.270	0.202	3.828	0.570	7.997	0.303

coefficient C_f are reported in Table 5.

It is worth noticing that the shape factors indicate that the boundary layer is in the laminar regime at $u_\infty = 5.27$ m/s, and in the turbulent regime at $u_\infty = 16.15$ m/s. In contrast, at the intermediate free-stream velocity, the boundary layer is not fully turbulent, but it is rather in the transitional regime (Bagheri and Stratiridakis, 1992).

The turbulent kinetic energy is well below $0.5 \times 10^{-3} u_\infty^2$ at $u_\infty = 5.27$ m/s, which confirms the laminar regime of the boundary layer at this free-stream velocity. Instead, it reaches peak values of $9 \times 10^{-3} u_\infty^2$ and $8 \times 10^{-3} u_\infty^2$ at the free-stream velocities of 10.58 m/s and 16.15 m/s, respectively. It may appear counterintuitive that the transitional boundary layer ($u_\infty = 10.58$ m/s) exhibits a higher turbulent kinetic energy peak than the turbulent boundary layer ($u_\infty = 16.15$ m/s). Upon close inspection of the instantaneous flow fields, it is noticed that in the

transitional case, the boundary layer fluctuates between a laminar (thinner boundary layer) and a turbulent (thicker boundary layer) state, thus resulting in higher fluctuations and therefore higher turbulent kinetic energy for $y < 3$ mm.

4.2. Experimental time-averaged velocity fields

The experimental time-averaged flow field at the three free-stream velocities is illustrated in Fig. 6. The incoming boundary layer separates at the leading edge of the cavity ($x/H = 0$), evolving into a curved shear layer that separates the outer potential-flow-like region and the recirculation region inside the cavity. Within the recirculation region, three focal points are identified, indicated with F_1 , F_2 and F_3 , respectively in Fig. 6. The focal point F_2 corresponds to the main recirculation region about the centre of the cavity, whereas focal points F_1 and F_3 are associated with the secondary vortices formed at the backward-facing and forward-facing edges of the cavity, respectively. The presence of both main recirculation region as well as secondary vortices is consistent with the results from Scarano et al. (1999) for the backward facing step flow. The locations of these focal points at the three free-stream velocities are summarised in Table 6. It is noticed that, for the lower free-stream velocity, the focal point F_1 located further away from both the

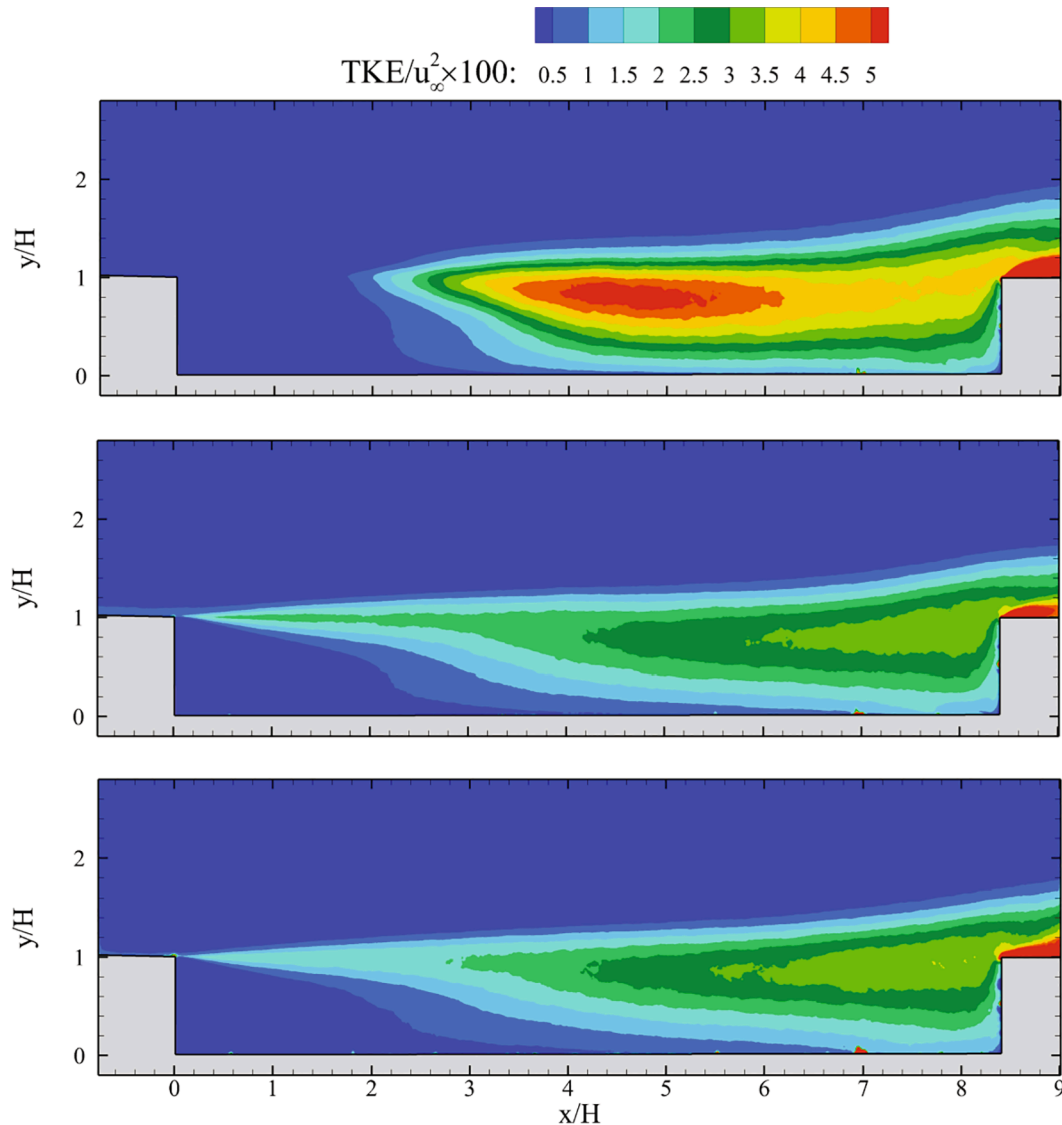


Fig. 7. Experimental turbulent kinetic energy TKE. Top: $u_\infty = 5.27$ m/s; middle: $u_\infty = 10.58$ m/s; bottom: $u_\infty = 16.15$ m/s.

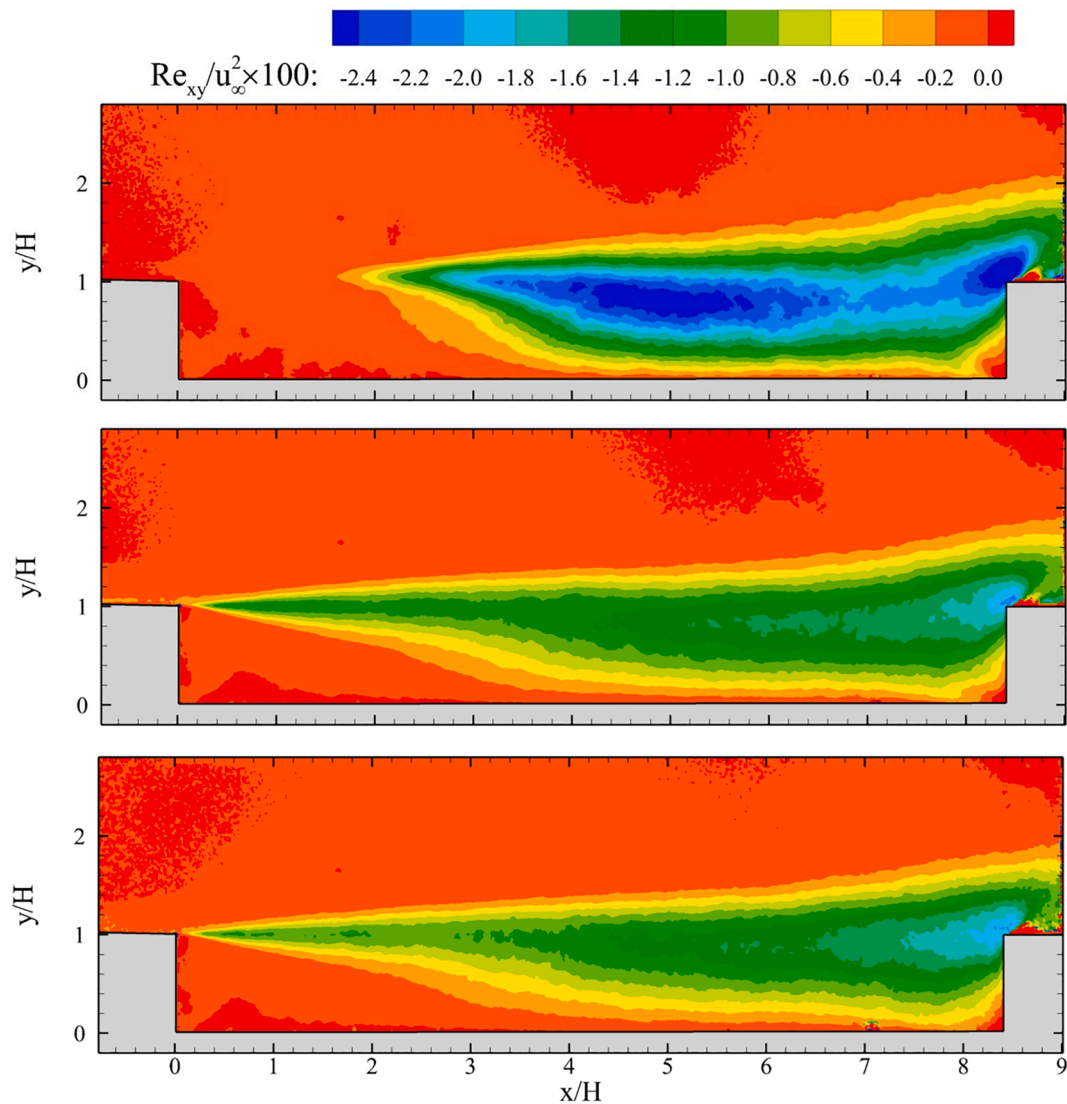


Fig. 8. Experimental Reynolds shear stress Re_{xy} . Top: $u_\infty = 5.27$ m/s; middle: $u_\infty = 10.58$ m/s; bottom: $u_\infty = 16.15$ m/s.

bottom and the backward facing cavity walls, when compared with the corresponding focal points at $u_\infty = 10.58$ m/s and 16.15 m/s. Also, the focal point F_2 is located further downstream in the $u_\infty = 5.27$ m/s case (x/H slightly exceed 4) than in the two other cases ($x/H < 4$). These results are attributed to the fact that, due to the laminar regime of the boundary layer before separation, the mixing process between outer and cavity regions occurs later at $u_\infty = 5.27$ m/s, thus shifting the main recirculation region further downstream. As a consequence of that, the secondary recirculation region close to the backward-facing edge also moves downstream and upwards. Concerning the third focal point F_3 , at $u_\infty = 5.27$ m/s it appears to be located closer to the bottom-right corner of the cavity than in the two other cases.

It is worth noticing that the flow does not reattach on the bottom wall of the cavity in any of the investigated cases. However, at $u_\infty = 5.27$ m/s the separating streamline gets relatively close ($y/H < 0.17$) to the bottom wall at $x/H = 7$, whereas in the other two cases it remains further away ($y/H > 0.35$) due to the presence of stronger secondary vortices close to the forward-facing edge.

4.3. Experimental turbulence kinetic energy and Reynolds shear stresses

Fig. 7 illustrates the turbulent kinetic energy measured experimentally at the three different free-stream velocities. Clear differences can be

seen between the lower velocity case and the two other cases. At the lower free-stream velocity of $u_\infty = 5.27$ m/s, the boundary layer before separation is in the laminar regime. As a consequence, it produces a laminar shear layer which undergoes instability around $x/H = 2$, thus yielding large velocity fluctuations in the main recirculation region ($TKE > 5\% u_\infty^2$). Conversely, at the two other free-stream velocities, the boundary layer prior to separation is turbulent, and non-zero TKE values are encountered in the shear layer right after separation. The presence of turbulent fluctuations in the shear layer of course augments the mixing process between the flow in the outer region and that in the cavity region, thus yielding a larger spread of the shear layer. At both 10.58 m/s and 16.15 m/s free-stream velocities, the turbulent kinetic energy within the cavity is lower than at $u_\infty = 5.27$ m/s, and does not exceed $3.5\% u_\infty^2$.

Finally, it is noted that the highest turbulent fluctuations at all velocities occur after the cavity ($x/H > 8.4$), close to the top wall. Those fluctuations are caused by the unsteady flow separation and reattachment at the top wall after the cavity, which is a known phenomenon for transitional cavity flows (Reulet et al., 2002).

The Reynolds shear stress fields are shown in Fig. 8. As for the turbulent kinetic distributions, the differences between the $u_\infty = 5.27$ m/s case and the higher free-stream velocity cases are prominent. In the $u_\infty = 5.27$ m/s case, the Reynolds shear stress attains small values ($|Re_{xy}/$

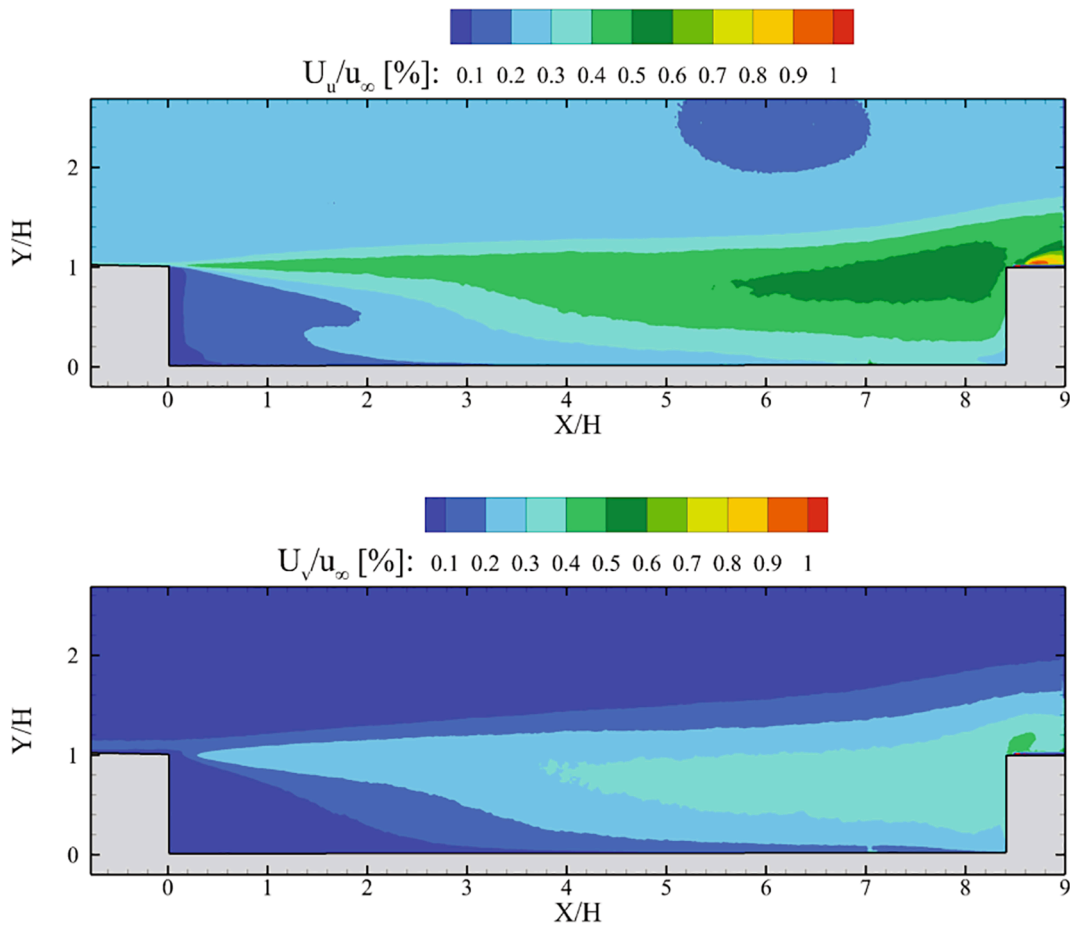


Fig. 9. Measurement uncertainty at 95% confidence level of the time-averaged velocity components for the $u_\infty = 10.58$ m/s case. Top: stream-wise velocity component; bottom: vertical velocity component.

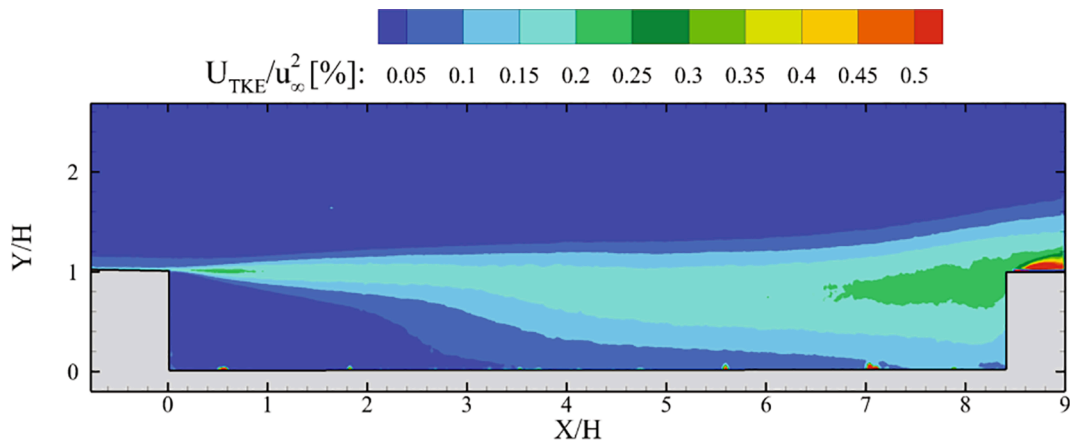


Fig. 10. Measurement uncertainty at 95% confidence level of the turbulent kinetic energy for the $u_\infty = 10.58$ m/s case.

$u_\infty^2 < 0.2 \times 10^{-2}$) up to $x/H = 2$, after which it rapidly increases inside the cavity up to non-dimensional values exceeding 2.5×10^{-2} . This result is ascribed to the laminar state of the separated shear layer, which undergoes transition to turbulence at $x/H = 2$, leading to large fluctuations beyond that location, and especially around the middle of the cavity ($4 \leq x/H \leq 6$) and close to its downstream top corner ($x/H = 8.4$). Instead, for the $u_\infty = 10.58$ m/s and $u_\infty = 16.15$ m/s cases, the Reynolds shear stress value starts increasing already from the separation point at the upstream edge of the cavity ($x/H = 0$). This behaviour is due to the turbulent state of the separating boundary layer. The maximum value of

$|Re_{xy}|/u_\infty^2$ is about 2.0×10^{-2} and is reached at the top corner of the cavity at its downstream edge.

4.4. Uncertainty bounds of the measured quantities

In this section, the 95% confidence level uncertainty of the time-averaged velocity components and of the turbulent kinetic energy are presented in Figs. 9 and 10, respectively, for the $u_\infty = 10.58$ m/s case. Similar uncertainty values are obtained for the $u_\infty = 5.27$ m/s and 16.15 m/s cases, and are omitted for sake of brevity.

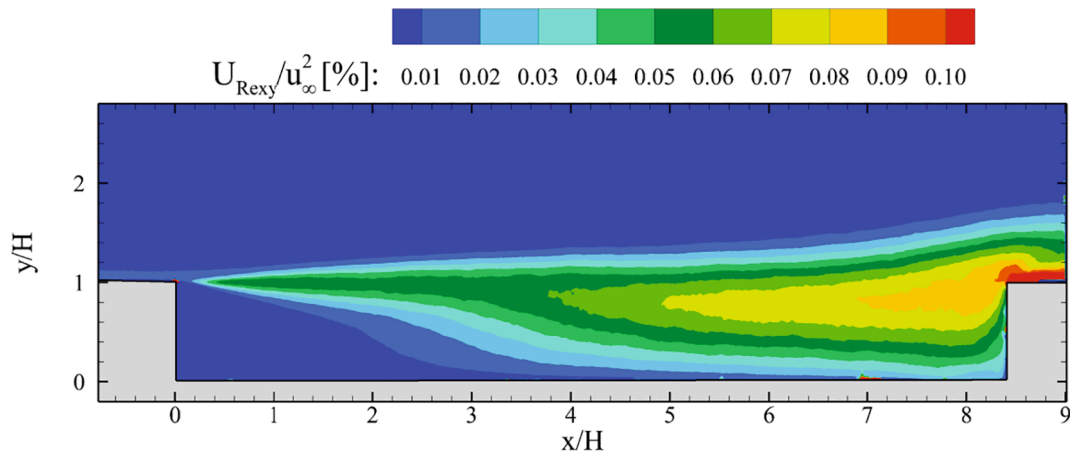


Fig. 11. Measurement uncertainty at 95% confidence level of the Reynolds shear stress for the $u_\infty = 10.58$ m/s case.

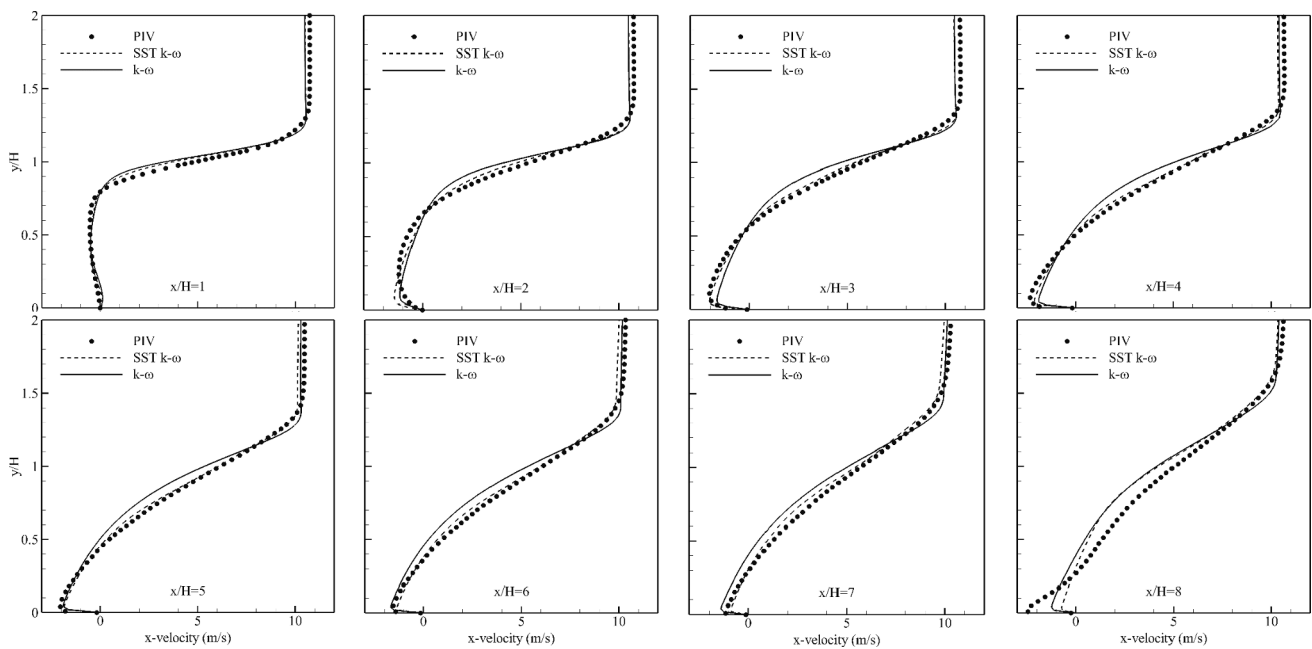


Fig. 12. Comparison between experimental and numerical time-averaged streamwise velocity profiles at different streamwise locations. Data for $u_\infty = 10.58$ m/s.

In the outer region, the flow behaves as a potential flow, with relatively low velocity gradients and out-of-plane particles motion; here the stream-wise velocity component \bar{u} features the lowest uncertainty, which is below 0.3% of u_∞ . Also in the recirculation region close to the backward-facing step ($x/H < 2$), the uncertainty of the stream-wise velocity does not exceed 0.3% of u_∞ , which is mainly ascribed to the low velocity in this region. The uncertainty increases up to 0.5% of u_∞ in the shear layer after separation, due to the high velocity gradients not fully resolved by the PIV processing algorithm, as well as the unsteadiness of the shear layer. Higher uncertainty occurs close to the forward-facing step ($6 < x/H < 8.4$), where the flow is highly turbulent and unsteady. The highest uncertainty ($U_{\bar{u}}/u_\infty \sim 1\%$) is found on the top wall after the cavity ($x/H > 8.4, y/H > 1$) because of the highly unsteady character of the flow in that region.

The uncertainty of the vertical velocity \bar{v} , presented in Fig. 9-bottom, shows similar spatial distribution as that of the stream-wise velocity component. Nevertheless, lower uncertainty values (below 0.4% of u_∞ inside the cavity, and up to 0.5% after the cavity) are retrieved as a consequence of the lower flow velocity in the vertical direction.

Also the uncertainty of the turbulent kinetic energy, illustrated in

Fig. 10, is the lowest in the outer flow region and in the recirculation region close to the backward-facing step; in fact, those are the regions where the flow exhibits the least unsteadiness. Higher uncertainty is retrieved in shear layer after separation, and close to the forward-facing step of the cavity. In the latter region, the uncertainty of the TKE attains 0.21% of u_∞^2 , which corresponds to 6% of the peak TKE value. After the cavity, U_{TKE} further increases exceeding 0.5% of u_∞^2 . Similarly, the uncertainty of the Reynolds shear stress, shown in Fig. 11 for the case $u_\infty = 10.58$ m/s, is below 0.1% of u_∞^2 in the potential flow region, as well as close to the bottom-left corner of the cavity. The uncertainty is higher ($\sim 0.05\%$ of u_∞^2) in the separated shear layer and further increases up to 0.09% of u_∞^2 close to the forward-facing edge of the cavity. The highest uncertainty of Re_{xy} is retrieved right after the cavity and exceeds 0.1% of u_∞^2 . Higher values of uncertainties, up to 0.15% of u_∞^2 , are retrieved inside the cavity for the $u_\infty = 5.27$ m/s case (not shown here).

4.5. Numerical models validation

In order to assess the reliability of the two RANS models used for numerical predictions, a comparison between results from CFD

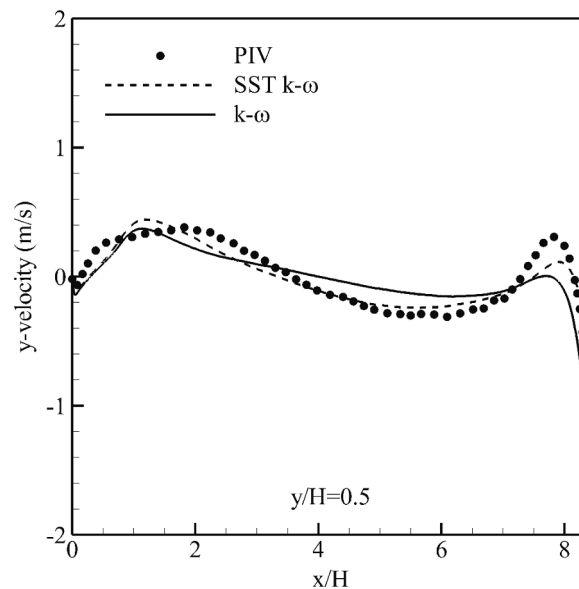


Fig. 13. Comparison between experimental and numerical time-averaged vertical velocity profiles at $y/H = 0.5$. Data for $u_\infty = 10.58$ m/s.

simulations and flow measurements by PIV is conducted at several representative profiles. The results for $u_\infty = 10.58$ m/s are summarized in Figs. 12 and 13.

The comparison shows a satisfactory agreement at all sections between experimental results and numerical predictions. Nevertheless, it is noticed that the SST $k-\omega$ turbulence model generally yields better agreement with the experimental data, especially in the shear layer region ($y/H \sim 1$), where the standard $k-\omega$ turbulence model underestimates the turbulent mixing and therefore predicts a thinner and sharper shear layer.

As expected, both the employed turbulence models satisfactorily predict the characteristics of the low-Reynolds flow under investigation, even though obtained results confirm that the SST $k-\omega$ demonstrates a superior ability to predict flow separation and a good behaviour in presence of adverse pressure gradients (Argyropoulos and Markatos, 2015).

Based on the above comparison, in the following only the results obtained with the SST $k-\omega$ turbulence model are considered for further comparisons with the experimental data. Besides, this model presented better performance in terms of convergence and stability. First, the flow topology and turbulent kinetic energy at the three-freestream velocities are analysed in Figs. 14 and 15, respectively, and compared with the measured ones, which have been discussed in Figs. 6 and 7. It is observed that the RANS simulations are able to correctly reproduce the time-averaged topology of the transitional cavity flow at the three Reynolds numbers. In particular, three foci are retrieved consistently with the PIV measurements. These foci correspond to the main recirculation region (F_2) and the secondary vortex structures close to the backward-facing and forward-facing edges of the cavity (F_1 and F_3 , respectively). The locations of the foci as obtained from the RANS simulations are reported in Table 7. Overall, the numerical predictions exhibit a good agreement with the experimental measurements. Nevertheless, the Reynolds number effects are much less pronounced than in the PIV measurements. In fact, the locations of the foci remain mainly unaltered when increasing the Reynolds number from 6300 to 19,000, whereas more significant variations were noticed in the PIV measurements, as discussed in Section 4.2.

Also the TKE contours, illustrated in Fig. 15, exhibit minor variations for varying Reynolds number. At all free-stream velocities, the turbulent kinetic energy starts increasing right after the separation point, reaching a value of $1.4\% u_\infty^2$ at $(x/H, y/H) = (1, 1)$ in the lowest free-stream

velocity case; at the same location and in the same free-stream case, the TKE from PIV measurements does not exceed $0.1\% u_\infty^2$. Within the cavity, the maximum TKE reaches $4\% u_\infty^2$ with small variations among the different Reynolds number cases; the PIV measurements, instead, reported a peak TKE exceeding $5\% u_\infty^2$ at the lowest free-stream velocity, and below $3.5\% u_\infty^2$ in the other cases. Finally, the numerical simulations correctly predict a peak of TKE of about $5\% u_\infty^2$ at the top-right corner of the cavity; however, the turbulent fluctuations decrease immediately after the cavity, contrary to the experimental measurements where they remain above $5\% u_\infty^2$.

Fig. 16 shows the experimental and numerical time-averaged streamwise velocity profiles at ten different sections of the cavity; the results are presented for the three free-stream velocities of 5.27 m/s, 10.58 m/s and 16.15 m/s. For the latter two free-stream velocities, the agreement between PIV measurements and CFD predictions is excellent. Differences between PIV and CFD data are noticeable only at the section downstream of the cavity ($x/H = 8.75$), where the PIV measurements over-estimate the flow velocity close to the wall. This result is ascribed to the finite spatial resolution of the PIV measurements. Conversely, the agreement at $u_\infty = 5.27$ m/s is less satisfactory. While the PIV measurements show a very thin shear layer up to $x/H = 2$, with a steep velocity increase between 0 m/s and the free-stream velocity at about $y/H = 1$, the numerical simulations predict a broader shear layer with a more gradual velocity variation along the vertical profiles. However, the agreement between numerical and experimental data improves at further downstream locations, especially after $x/H = 4$.

The TKE profiles, illustrated in Fig. 17, exhibit larger discrepancies between numerical simulations and experiments. In particular, at $u_\infty = 5.27$ m/s, the CFD simulation over-predicts the turbulent fluctuations in the separating boundary layer, resulting in higher TKE in the shear layer right after separation ($x/H = 1$ and 2). Conversely, the PIV measurements report null turbulent kinetic energy at $x/H = 1$ due to the laminar regime of the separating boundary layer. Further downstream, the numerical simulation under-predicts the turbulence mixing in the shear layer, thus returning lower TKE values than the flow measurements. The larger deviations occur on the top wall after the cavity, where the simulation under-predicts the turbulent kinetic energy close to the solid surface.

At the two other free-stream velocities, namely $u_\infty = 10.58$ m/s and 16.15 m/s, instead, the numerical and experimental TKE profiles agree very well in the shear layer between the separation point and $x/H = 2$.

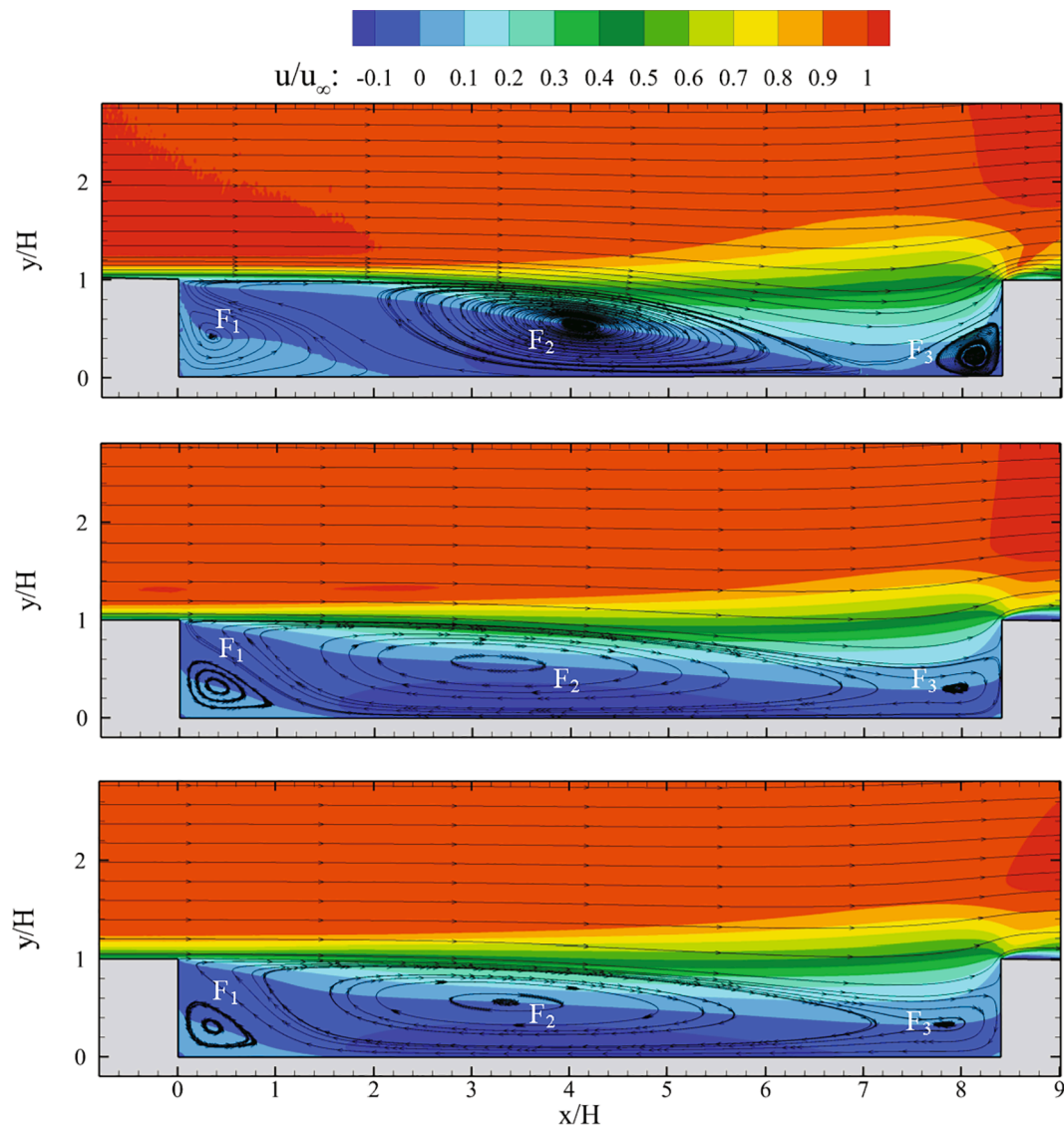


Fig. 14. Time-averaged velocity fields from RANS simulations with the SST $k-\omega$ turbulence model. Top: $u_\infty = 5.27$ m/s; middle: $u_\infty = 10.58$ m/s; bottom: $u_\infty = 16.15$ m/s.

For $x/H \geq 3$, instead, the numerical simulations over-estimate the turbulent fluctuations, with larger discrepancies encountered at the higher free-stream velocity. Also in these two cases, the larger differences take place after the cavity, where the measured TKE values close to the wall exceed those predicted by CFD simulations.

To explain the differences between the TKE values obtained by PIV measurements and CFD simulations especially downstream of the cavity, two instantaneous flow fields are shown in Fig. 18 for the case of free-stream velocity of 10.58 m/s. In the field of Fig. 18-top, the separated shear layer originating from the top-left corner of the cavity impinges on the forward-facing surface of the cavity at $x/H = 8.4$. As a consequence, the flow just downstream of the cavity ($x/H > 8.4$) is fully attached and the velocity attains values close to the free-stream value. Conversely, in the field of Fig. 18-bottom the separated shear layer does not reattach within the cavity, and the streamwise velocity component downstream of the cavity is negative up to $-0.1 u_\infty$. Hence, in the latter region the flow velocity varies from negative to the free-stream value, thus resulting in large Reynolds normal stresses. Apparently, this effect is not captured by the numerical simulations, thus yielding a noticeable difference between the turbulent kinetic energy values from measurements and simulations.

5. Conclusions

A benchmark experimental database for the transitional cavity flow is presented, obtained by two-dimensional two-component PIV measurements. The database is primarily meant for the validation of low-fidelity CFD simulations. The measurements are conducted at Reynolds numbers between 6300 and 19,000 based on the height of the cavity, encompassing the cases of laminar and turbulent boundary layer regimes prior to separation. Numerical simulations of the transitional cavity flow are also conducted via RANS simulations using two different turbulent models, namely standard $k-\omega$ and SST $k-\omega$.

The experimental results showed the presence of a main recirculation region and two secondary vortices inside the cavity, located close to the backward-facing and forward-facing cavity edges, respectively. The location and extent of these vortical regions are Reynolds number dependent, and vary based on the regime of the boundary layer before separation. In all the investigated cases, the separating flow does not reattach on the bottom wall of the cavity, but rather on the cavity forward-facing edge. The reattachment is highly unsteady, as demonstrated by the large turbulent kinetic energy values in this region.

From the comparison between CFD simulations and experimental results, it is concluded that the SST $k-\omega$ turbulence model yields more

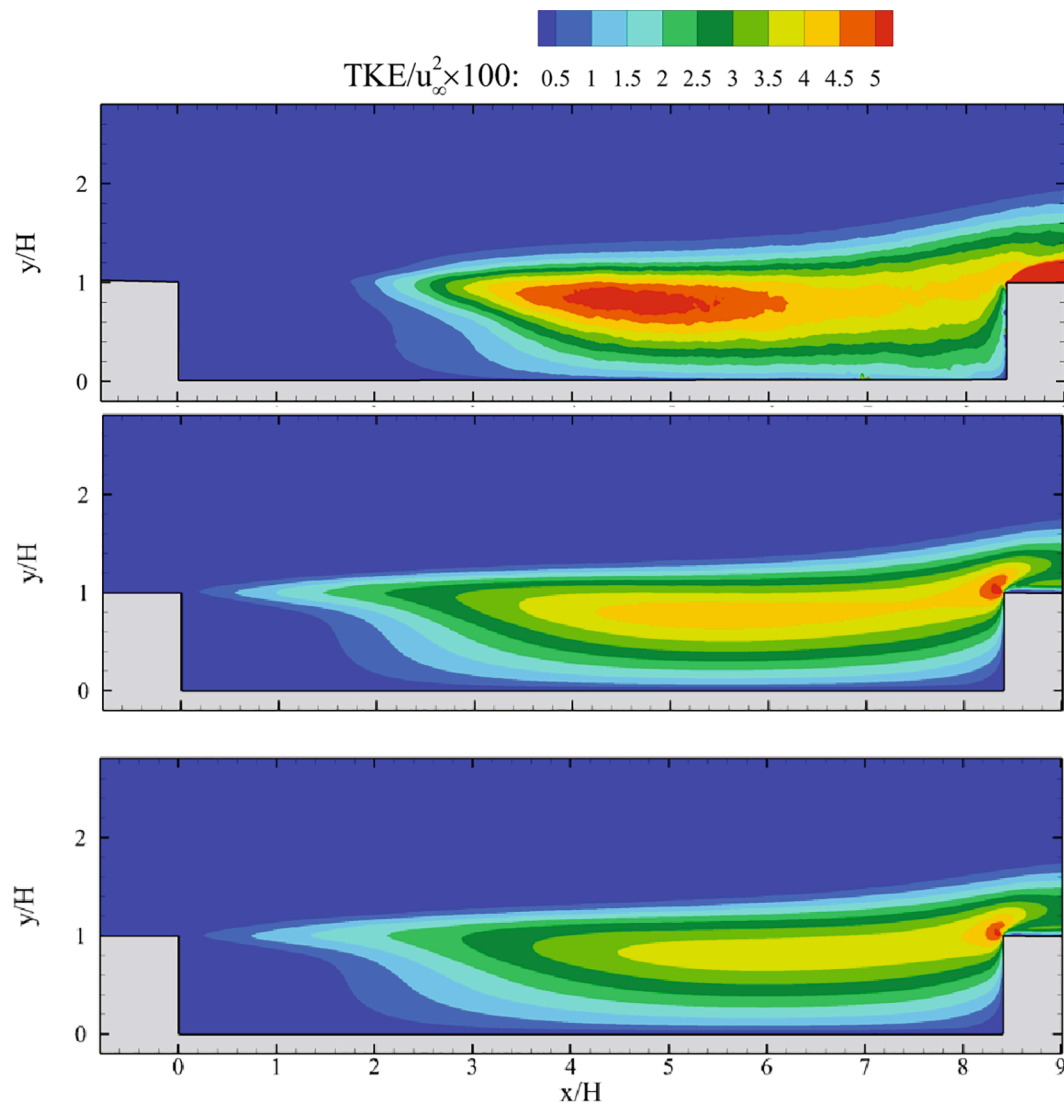


Fig. 15. Turbulence kinetic energy TKE from RANS simulations with the SST $k-\omega$ turbulence model. Top: $u_\infty = 5.27$ m/s; middle: $u_\infty = 10.58$ m/s; bottom: $u_\infty = 16.15$ m/s.

Table 7

Locations of the three foci at the three free-stream velocities. RANS simulations with the SST $k-\omega$ turbulence model.

u_∞ (m/s)	F_1		F_2		F_3	
	x/H	y/H	x/H	y/H	x/H	y/H
5.27	0.418	0.332	3.163	0.562	7.967	0.303
10.58	0.386	0.320	3.266	0.557	7.960	0.308
16.15	0.356	0.313	3.350	0.560	7.846	0.332

accurate flow predictions than the standard $k-\omega$ turbulence model, especially in the shear layer region. The agreement between numerical and experimental data is particularly good in terms of time-averaged flow field at the higher free-stream velocities. Larger discrepancies are found at the lower free-stream velocity, in particular in the shear layer right after flow separation. Overall, it is concluded that the numerical simulations do not capture the variations of the flow field, and in particular of the locations of the vortical structures, for varying Reynolds number. For what concerns the turbulent kinetic energy, the agreement is less satisfactory, with the simulations under-predicting the turbulent fluctuations in the main recirculation region at $u_\infty = 5.27$ m/s, and over-predicting them at the higher free-stream velocities. The larger

discrepancies are found downstream of the cavity, where the simulations under-estimate the unsteadiness of the flow reattachment.

Future research will involve performing high-fidelity simulations on the same test case to assess the relative influence of the accuracy of the boundary conditions and of the employed turbulence models (considering both RANS and LES simulations) on the agreement between numerical and experimental data.

CRedit authorship contribution statement

A. Sciacchitano: Project administration, Methodology, Supervision. **F. Arpino:** Investigation, Conceptualization, Software, Methodology. **G.**

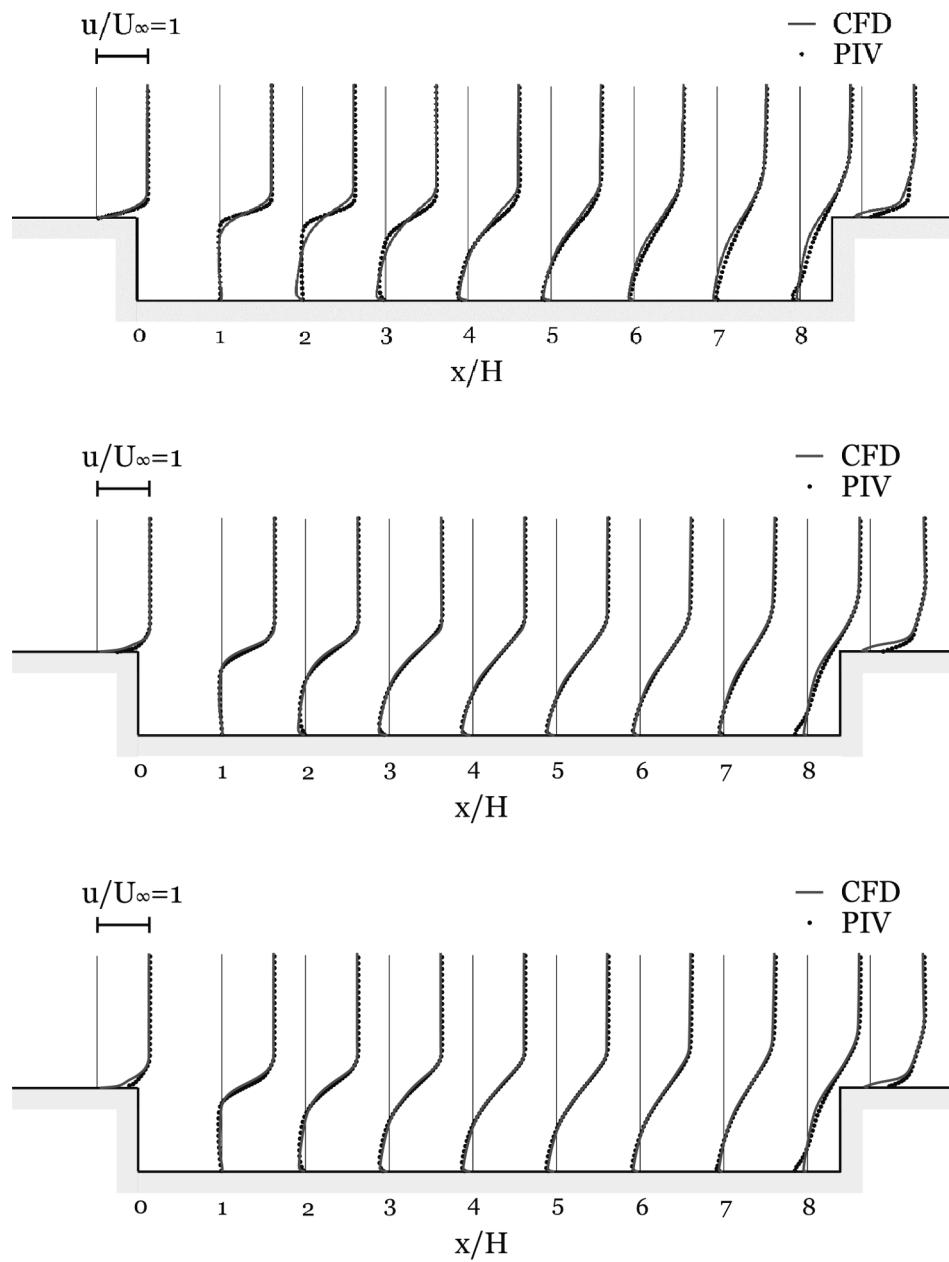


Fig. 16. Comparisons between the SST $k-\omega$ and the PIV measurements: time-average streamwise velocity profiles at ten different streamwise locations. Top: $u_\infty = 5.27$ m/s; middle: $u_\infty = 10.58$ m/s; bottom: $u_\infty = 16.15$ m/s.

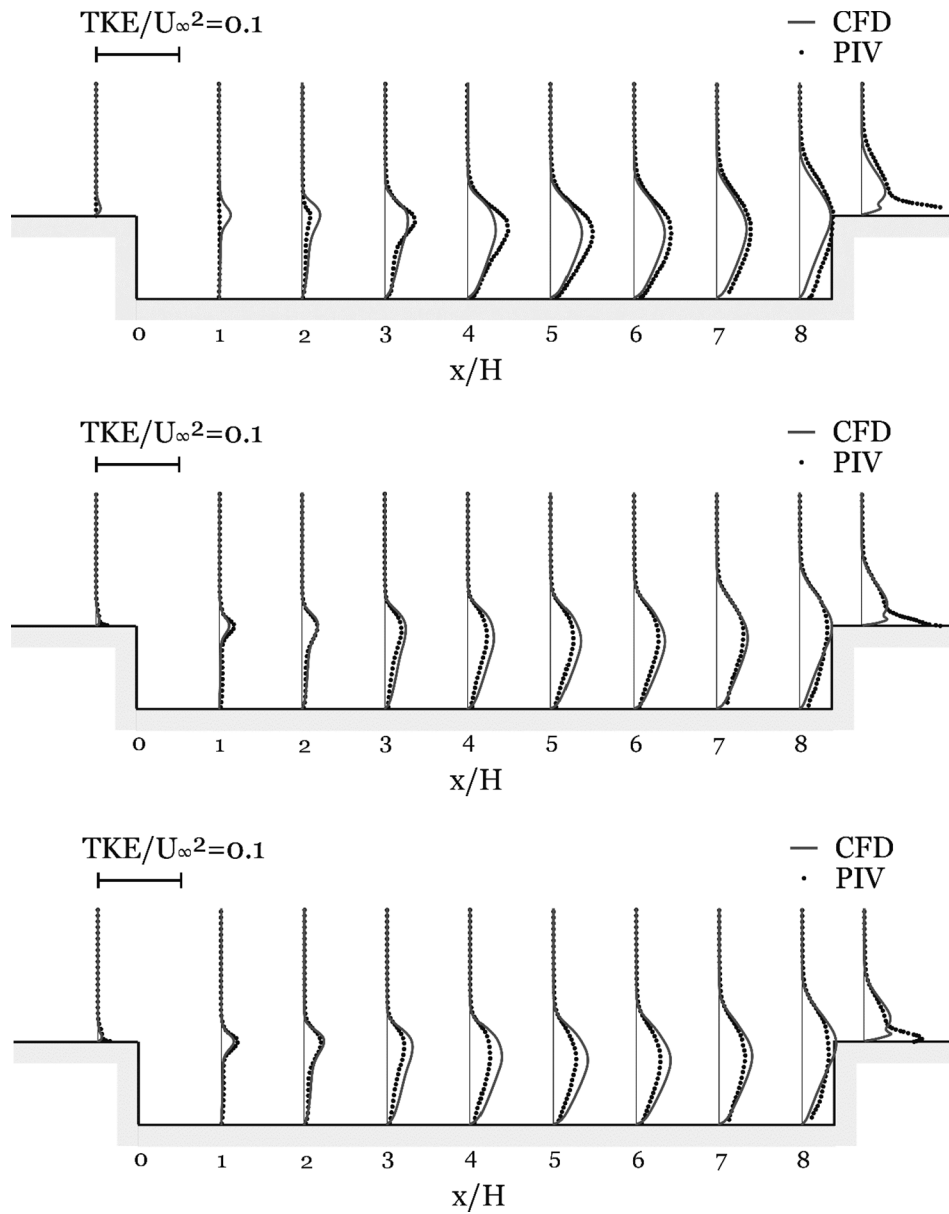


Fig. 17. Comparisons between the SST $k-\omega$ and the PIV measurements: TKE profiles at ten different streamwise locations. Top: $u_\infty = 5.27$ m/s; middle: $u_\infty = 10.58$ m/s; bottom: $u_\infty = 16.15$ m/s.

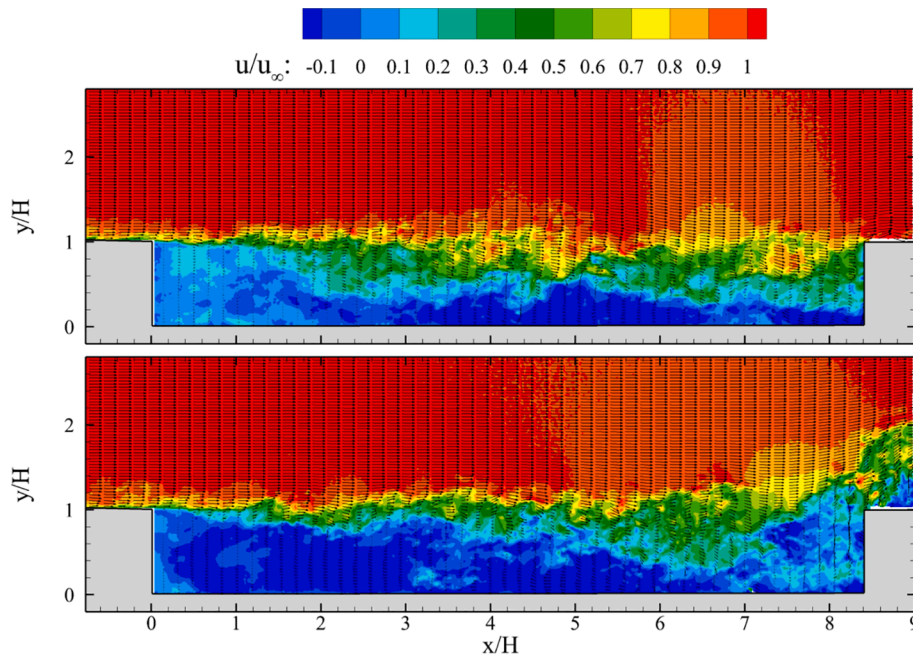


Fig. 18. Two instantaneous velocity fields measured by PIV for the $u_\infty = 10.58$ m/s case. In the top field, the flow downstream of the cavity is fully attached, whereas in the bottom field it is separated.

Cortellessa: Data curation, Validation, Software.

Declaration of Competing Interest

The authors declare that they have no known competing financial interests or personal relationships that could have appeared to influence the work reported in this paper.

Appendix A. Supplementary data

Supplementary data to this article can be found online at <https://doi.org/10.1016/j.ijheatfluidflow.2021.108831>.

References

- Adrian, R.J., 1997. Dynamic ranges of velocity and spatial resolution of particle image velocimetry. *Measur. Sci. Technol.* 8 (12), 1393–1398. <https://doi.org/10.1088/0957-0233/8/12/003>.
- Argyropoulos, C.D., Markatos, N.C., 2015. Recent advances on the numerical modelling of turbulent flows. *Appl. Math. Modell.* 39 (2), 693–732. <https://doi.org/10.1016/j.apm.2014.07.001>.
- Arpino, F., Fernicola, V., Frattolillo, A., Rosso, L., 2009. A CFD study on a calibration system for contact temperature probes. *Int. J. Thermophys.* 30 (1), 306–315. <https://doi.org/10.1007/s10765-008-0451-8>.
- Arpino, F., Cortellessa, G., Dell'Isola, M., Massarotti, N., Mauro, A., 2014. High order explicit solutions for the transient natural convection of incompressible fluids in tall cavities. *Numer. Heat Transfer Part A Appl.* 66 (8), 839–862. <https://doi.org/10.1080/10407782.2014.892389>.
- Arpino, F., Cortellessa, G., Frattolillo, A., 2015. Experimental and numerical assessment of photovoltaic collectors performance dependence on frame size and installation technique. *Sol. Energy* 118, 7–19. <https://doi.org/10.1016/j.solener.2015.05.006>.
- Arpino, F., Cortellessa, G., Dell'Isola, M., Scungio, M., Focanti, V., Profili, M., Rotondi, M., 2017. CFD simulations of power coefficients for an innovative Darrieus style vertical axis wind turbine with auxiliary straight blades. *J. Phys. Conf. Ser.* 923, 012036. <https://doi.org/10.1088/1742-6596/923/1/012036>.
- Atvars, K., Knowles, K., Ritchie, S.A., Lawson, N.J., 2009. Experimental and computational investigation of an “open” transonic cavity flow. *Proc. Inst. Mech. Eng. Part G J. Aerosp. Eng.* 223 (4), 357–368. <https://doi.org/10.1243/09544100JAERO445>.
- Bagheri, N., Stratiridakis, C.J., White, B.R., 1992. Measurements of turbulent boundary layer Prandtl numbers and space-time temperature correlations. *AIAA J.* 30 (1), 35–42. <https://doi.org/10.2514/3.10879>.
- Bengoechea, Antón, R., Larraona, G.S., Ramos, J.C., Rivas, A., 2014. Influence of geometrical parameters in the downstream flow of a screen under fan-induced swirl conditions. *Eng. Appl. Comput. Fluid Mech.* 8 (4), 623–638. <https://doi.org/10.1080/19942060.2014.11083312>.
- Boomsma, A., Bhattacharya, S., Troolin, D., Pothos, S., Vlachos, P., 2016. A comparative experimental evaluation of uncertainty estimation methods for two-component PIV. *Meas. Sci. Technol.* 27 (9). <https://doi.org/10.1088/0957-0233/27/9/094006>.
- Botella, O., Peyret, R., 1998. Benchmark spectral results on the lid-driven cavity flow. *Comput. Fluids* 27 (4), 421–433. [https://doi.org/10.1016/S0045-7930\(98\)00002-4](https://doi.org/10.1016/S0045-7930(98)00002-4).
- Coleman, H.W., Steele, W.G., 2018. *Experimentation, Validation, and Uncertainty Analysis for Engineers*. Wiley.
- Davis, R.S., 1992. Equation for the determination of the density of moist air (1981/91). *Metrologia* 29 (1), 67–70. <https://doi.org/10.1088/0026-1394/29/1/008>.
- DeBonis, J.R., Oberkampf, W.L., Wolf, R.T., Orkwis, P.D., Turne, M.G., Babinsky, H., 2010. Assessment of CFD models for shock boundary-layer interaction. In: *AIAA Appl Aerodyn. Conf.*. <https://doi.org/10.2514/6.2010-4823>.
- Fincham, A.M., Spedding, G.R., 1997. Low cost, high resolution DPIV for measurement of turbulent fluid flow. *Exp. Fluids* 23 (6), 449–462. <https://doi.org/10.1007/s003480050135>.
- Ford, M.D., et al., 2008. PIV-measured versus CFD-predicted flow dynamics in anatomically realistic cerebral aneurysm models. *J. Biomech. Eng.* 130 (2). <https://doi.org/10.1115/1.2900724>.
- Foucaut, J.M., Carlier, J., Stanislas, M., 2004. PIV optimization for the study of turbulent flow using spectral analysis. *Meas. Sci. Technol.* 15 (6), 1046–1058. <https://doi.org/10.1088/0957-0233/15/6/003>.
- Ghia, U., Ghia, K.N., Shin, C.T., 1982. High-Re solutions for incompressible flow using the Navier-Stokes equations and a multigrid method. *J. Comput. Phys.* 48 (3), 387–411. [https://doi.org/10.1016/0021-9991\(82\)90058-4](https://doi.org/10.1016/0021-9991(82)90058-4).
- Harris, A., Harris, S., Rauls, D., 2016. Numerical experiments using MATLAB: superconvergence of nonconforming finite element approximation for second-order elliptic problems. *Appl. Math.* 07 (17), 2174–2182. <https://doi.org/10.4236/am.2016.717173>.
- Lewis, R.W., Nithiarasu, P., Seetharamu, Kankanhalli N., 2004. *Fundamentals of the Finite Element Method for Heat and Fluid Flow*. Wiley.
- Menter, F.R., 1993. Zonal two equation $k-\omega$ turbulence models for aerodynamic flows. In: *presentato al AIAA 23rd Fluid Dynamics, Plasmadynamics, and Lasers Conference, 1993, Consultato: lug. 06, 1993*. [Online]. Disponibile su: <<https://www.scopus.com/inward/record.uri?eid=2-s2.0-84995453152&partnerID=40&md5=05f6f9f883d6f842282b9db4dc7b7387>>.
- Neal, D.R., Sciacchitano, A., Smith, B.L., Scarano, F., 2015. Collaborative framework for PIV uncertainty quantification: the experimental database. *Meas. Sci. Technol.* 26 (7). <https://doi.org/10.1088/0957-0233/26/7/074003>.
- Nogueira, J., Lecuona, A., Rodríguez, P.A., 2005. Limits on the resolution of correlation PIV iterative methods. *Fund. Exp. Fluids* 39 (2), 305–313. <https://doi.org/10.1007/s00348-005-1016-2>.
- Oberkampf, W.L., Roy, C.J., 2011. In: *Verification and Validation in Scientific Computing*. Cambridge University Press, p. 767.
- Prasad, A.K., Koseff, J.R., 1989. Reynolds number and end-wall effects on a lid-driven cavity flow. *Phys. Fluids A* 1 (2), 208–218. <https://doi.org/10.1063/1.857491>.
- Raffel, M., Willert, C., Wereley, S., Kompenhans, J., 2007. *Particle Image Velocimetry – A Practical Guide*, second ed.
- Raffel, M., Willert, C.E., Scarano, F., 2018. *Particle Image Velocimetry*. Springer International Publishing.

- Reulet, P., Esteve, M.J., Millan, P., Riethmuller, M.L., 2002. Experimental characterization of the flow within a transitional rectangular cavity. *J. Flow Visualization Image Process.* 9 (2-3), 18. <https://doi.org/10.1615/JFlowVisImageProc.v9.i2-3.50>.
- Roache, P.J., 1997. In: *Quantification of Uncertainty in Computational Fluid Dynamics*. Annual Reviews Inc., p. 160.
- Scarano, F., Benocci, C., Riethmuller, M.L., 1999. Pattern recognition analysis of the turbulent flow past a backward facing step. *Phys. Fluids* 11 (12), 3808–3818. <https://doi.org/10.1063/1.870240>.
- Scarano, F., Riethmuller, M.L., 2000. Advances in iterative multigrid PIV image processing. *Exp. Fluids* 29 (7), S051–S060.
- Sciacchitano, A., 2019. Uncertainty quantification in particle image velocimetry. *Meas. Sci. Technol.* 30 (9) <https://doi.org/10.1088/1361-6501/ab1db8>.
- Sciacchitano, A., Wieneke, B., 2016. PIV uncertainty propagation. *Meas. Sci. Technol.* 27 (8) <https://doi.org/10.1088/0957-0233/27/8/084006>.
- Scungio, M., Arpino, F., Cortellessa, G., Buonanno, G., 2015. Detached eddy simulation of turbulent flow in isolated street canyons of different aspect ratios. *Atmos. Pollut. Res.* 6 (2), 351–364. <https://doi.org/10.5094/APR.2015.039>.
- Sheng, J., Meng, H., Fox, R.O., 1998. Validation of CFD simulations of a stirred tank using particle image velocimetry data. *Can. J. Chem. Eng.* 76 (3), 611–625. <https://doi.org/10.1002/cjce.5450760333>.
- Smith, B.L., 2017. The difference between traditional experiments and CFD validation benchmark experiments. *Nucl. Eng. Des.* 312, 42–47. <https://doi.org/10.1016/j.nucengdes.2016.10.007>.
- Stanislas, M., Westerweel, J., Kompenhans, J., 2004. *Particle Image Velocimetry: Recent Improvements*. Springer.
- Versteeg, H.K., Malalasekera, W., 2007. *An Introduction to Computational Fluid Dynamics: The Finite Volume Method*. Prentice Hall.
- Westerweel, J., 1997. Fundamentals of digital particle image velocimetry. *Meas. Sci. Technol.* 8 (12), 1379–1392. <https://doi.org/10.1088/0957-0233/8/12/002>.
- Westerweel, J., Elsinga, G.E., Adrian, R.J., 2013. Particle image velocimetry for complex and turbulent flows. *Annu. Rev. Fluid Mech.* 45, 436.
- Wilcox, D.C., 2008. Formulation of the $k-\epsilon$ turbulence model revisited. *AIAA J.* 46 (11), 2823–2838. <https://doi.org/10.2514/1.36541>.
- Wilson, B.M., Smith, B.L., 2013. Uncertainty on PIV mean and fluctuating velocity due to bias and random errors. *Meas. Sci. Technol.* 24 (3) <https://doi.org/10.1088/0957-0233/24/3/035302>.